# Tomographic Shadowgraphy of Swirled non-reactive Spray Injection in a Generic Aero Engine Burner under Realistic Operating Conditions

Joachim Klinner[*,1], Stefan Freitag[1], Christoph Hassa[1], Christian Willert[1]

[1]Institute of Propulsion Technology, German Aerospace Center (DLR), 51170 Köln, Germany

*Corresponding author: joachim.klinner@dlr.de

## Abstract

This contribution describes the application of tomographic shadowgraphy to measure instantaneous velocities of droplets undergoing airblast-atomization in the non-reactive flow of a generic aero engine burner model at Weber numbers of $We_{aero} = 360 - 770$, air pressures of $p_a = 4 - 7$ bar and air temperatures of $T_a = 440 - 570$ K. The burner employs air-blast atomization of a single jet in cross-flow in the main stage. The measurement setup is described in detail and the depth-of-field with respect to droplet size is estimated. The latter was calculated on the basis of Mie simulations and calibration data of the point-spread function. At a given volume size of $16 \times 13 \times 10$ mm$^3$ it turned out that the minimum resolvable droplet diameter reduces down to $d = 10$ $\mu$m within the focus and increases up to $d = 10 - 20$ $\mu$m towards the volume edges. Velocities of droplets above the resolution limit were retrieved by 3D correlation of two volumetric reconstructions recorded at consecutive time-steps. Extracted slices of the instantaneous axial velocity indicate strong motion and fluctuations of the spray tail with increasing temperature and Weber number. Validation against PDA data revealed good agreement at size classes $d = 10$ $\mu$m, $15$ $\mu$m. Slight deviations occur in regions with strong velocity gradients probably due to the presence of reconstruction ambiguities (ghost particles).

## Introduction

The optimization of aero engine combustors requires a detailed knowledge of the fuel atomization process including fuel placement, breakup length scales, spray penetration depth, droplet sizes and velocities. Providing relevant experimental data on swirled air-blast atomization on the other hand raises some serious challenges such as deployment of realistic operating conditions and sufficient optical access. Another obstacle is that the dispersion of liquid kerosine by swirling air-blast atomizers is driven by a highly three-dimensional flow. Liquid jet breakup itself is unsteady due to turbulence of the surrounding gas respectively of the liquid. Therefore, a better insight into the phenomenon can be provided by diagnostic methods capable of mapping the instantaneous three-dimensional velocity and placement of atomized fuel within the combustion volume both spatially and temporally.

One possible spray imaging technique could be tomographic shadowgraphy which is capable of reconstructing the three dimensional instantaneous spray distributions and droplet velocities within a given volume. The method is based on a multiple view imaging setup with inline illumination provided by current-pulsed LEDs allowing the droplet shadows to be projected onto multiple sensor planes. This technique has previously only been applied with good optical accessibility to hollow cone and flat fan sprays at ambient conditions [1]. This contribution describes a feasibility study on the application of tomo shadowgraphy under rough operating conditions in a non-reacting kerosine spray in a high pressure environment and with preheated airflow.

The contribution describes various aspects of the adaption of the tomographic setup to the facility. The depth of field of the measurement setup is estimated from shadow imaging models provided in the literature combined with calibration data of the point-spread function with the latter characterizing the resolution capabilities of the multiple view setup. After tomographic reconstruction of the volumetric intensity distribution, droplet velocities are obtained by 3D correlation of small interrogation volumes at two consecutive time steps as known from conventional tomographic particle image velocimetry [2]. In comparison to tomographic PIV which assumes an even distribution of particles within the volume, sprays generally exhibit pronounced local variations of droplet number density and size. Of particular interest to spray investigation is the near field where the fragments of the kerosine jet leave the annular gap of the burner plate. The present application of tomographic shadowgraphy intends to provide insight into the instantaneous spray tail trajectory and extension.

## Test facility and operation conditions

Measurements are performed in a non-reactive kerosine-air flow in the optical swirling spray injector test rig (OSSI) at the DLR Center in Cologne [3]. Fig. 1 shows a longitudinal section of the test rig. The spray chamber has a length of $200$ mm and a square cross-section of internal width of $102$ mm. The burner is supplied with preheated and pressurized air through an upstream plenum and baffle. The kerosine supply line passes through the preheated air flow and thus kerosine is preheated prior to injection to temperatures provided in Table 1. An exchangeable critical nozzle downstream of the spray chamber provides mass flow control at different pressure levels. Pressure windows
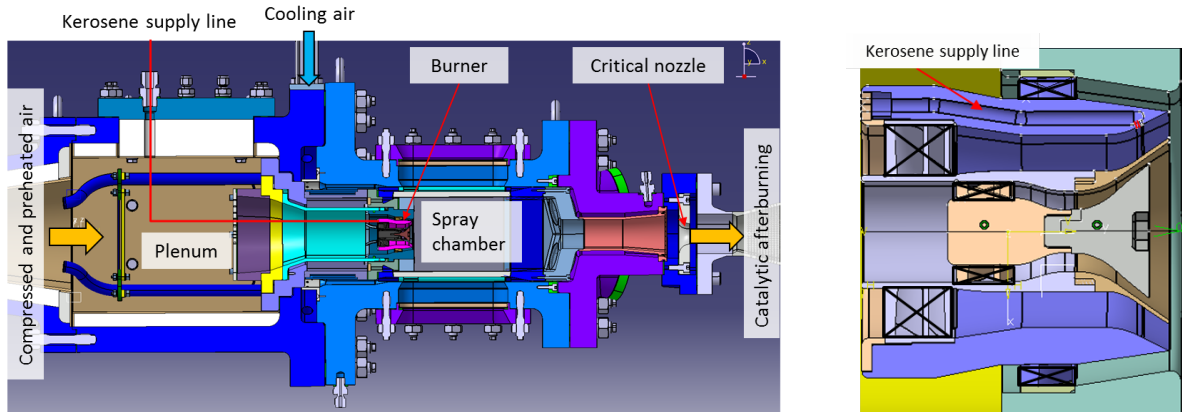
**Figure 1.** Schematic of the optical swirling spray injector test rig (*left*) and generic burner with swirl generators(*right*)(c.f. [3])
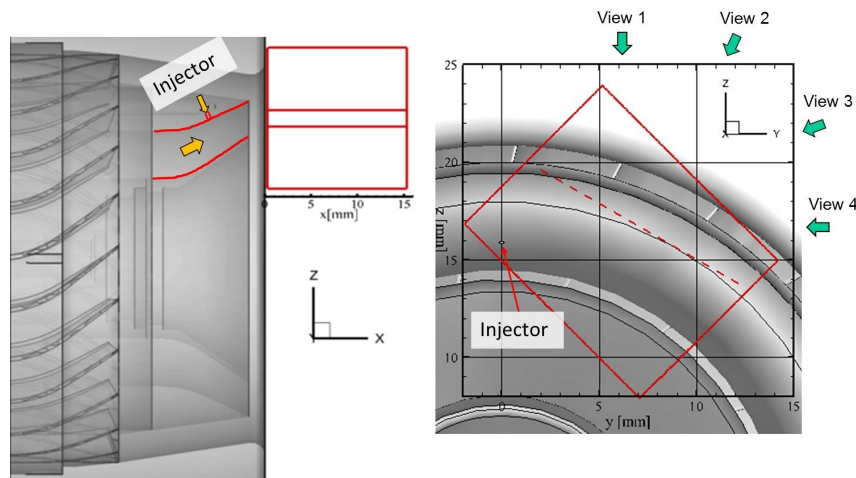


**Figure 2.** Orientation of the measurement volume; *left* side view with annular passage and injector; *right* axial view of the measurement volume; PDA measurements were performed along the dashed line

of 35 mm thickness and liner windows of 7 mm thickness provide optical access to the test-section from four sides. Cooling air is blown through the gap between pressure and liner window to protect the glass from thermal loading and to keep the external pressure casing at ambient temperature levels. The test rig design and the generic burner model geometry are described in detail in [3].

The generic burner employs air-blast atomization of a single jet in cross-flow in the main stage. Kerosine is injected through a single bore of 0.88 mm length and a diameter of 0.29 mm (L/D=3). The injector is located in a conical main module which is placed between two co-rotating swirl generators. A liquid jet of kerosine is injected orthogonal to the conical surface. Downstream, the liquid jet fragments propagate in swirl direction and leave the burner plate through an annular passage at a axial distance of 6 mm from the injector (c.f. Fig. 2,left).

During the experiments described herein the pressure inside the spray chamber was varied between 4 and 7 bar and the burner air flow was preheated in a range between 440 K and 570 K. The liquid-to-air momentum flux ratio is kept constant while the aerodynamic Weber number ranges from 360 at base line conditions to 770. Table 1 summarizes the operation conditions.

Estimation of the Weber number is based on slightly cooler kerosine temperatures measured about 5 mm upstream of the injection port and therefore might be slightly underestimated due to an overestimation of kerosine surface tension.

**Measurement techniques**

Tomographic shadowgraphy [1] has been applied to a measurement volume of $16 \times 13 \times 10$ mm$^3$ which is located in the vicinity of the burner plate 6 mm downstream of the injection bore (c.f. Fig. 2). The experimental setup for tomographic shadowgraphy outlined in Fig. 3 and Fig. 4 involves four synchronized double frame cameras (ILA.sCMOS) angled with $-45°$, $-20°$, $25°$ and $45°$ acquiring double-images at a frame rate of 20 Hz. All cameras are equipped with macro lenses (Nikkor Micro) at magnifications of approximately M=0.86 or 7.6 $\mu$m/pixel at image
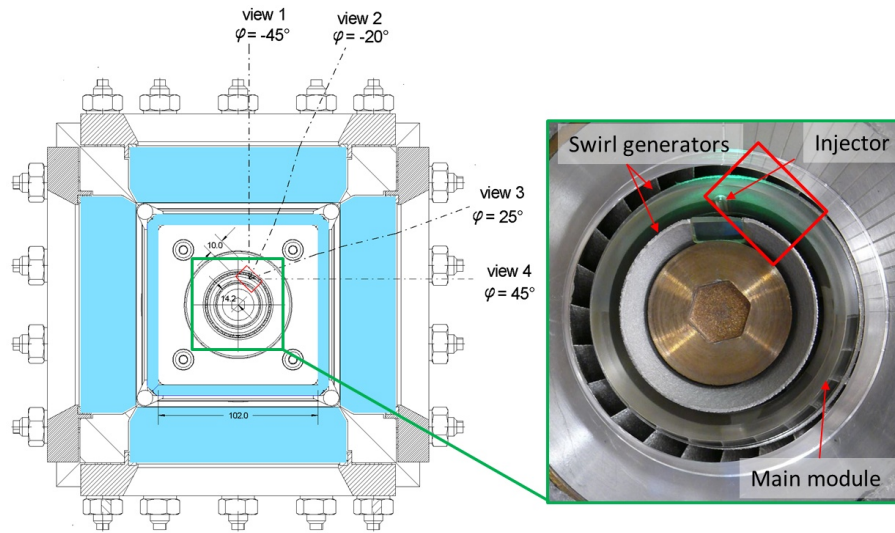
**Figure 3.** Test section of the optical swirling spray injector rig; *Left* Camera orientation and volume of interest (red box); *Right* generic burner with a transparent main module (used for spray visualization) and injector bore

sizes of $2560 \times 2160$ pixel. The two outer cameras use lenses of $f = 105$ mm focal length and $35$ mm close-up extension rings. Due to the oblique view through the liner and pressure windows ($42$ mm thickness in total), droplet images of the inner cameras exhibit astigmatism or elliptic distortions. Therefore additional compensator windows of similar thickness are mounted in front of the inner cameras to minimize these distortions (see Fig. 4, right). These compensator windows generate similar elliptical droplet image distortions which are rotated around the optical axis by $90°$ compared to image distortions from pressure windows which leads to a near cancelation of droplet image ellipticity. The two inner cameras are both equipped with $f = 200$ mm lenses in order to accommodate the additional compensator plates in the optical path.

With the aid of Scheimpflug (tilt) camera mounts, the focal planes of the cameras are aligned with the calibration target positioned at the center of the imaged volume. This ensures that all cameras share a similar depth of field. All apertures are stopped down to $f_\# = 22$ to maintain a depth of field of approximately $10$ mm. Estimations of droplet visibility along volume depth are reported in the following section.

Inline illumination is provided for each camera by a current-pulsed, high power green LED (Luminus, SST-90, green) whose light is collimated with an aspheric condenser lens of $f = 30$ mm [4]. Peak currents of $I_{f,max} = 27$ A at $\tau_p = 400$ ns were found sufficient to provide bright-field intensity levels at $5\%$ of the camera dynamic range (16bit) at lens apertures $f_\# = 22$ and a magnification close to 1. The pulse separation was $\Delta t = 1.7$ $\mu$s to achieve droplet image displacements in the order of $10$ pixel.

Volume calibration is achieved with lithographic photomasks of checkerboard patterns on soda-lime glass that are backlit with a display LED for homogenous illumination. Opaque regions consist of a $100$ nm thick layer of chromium oxide and have a lateral dimensional tolerance of $\pm300$ nm. The traversal of the calibration target along z-axis by a motorized translation stage (Newport Agilis) allows the sequential recording of 3-D points in space at a manufacturer specified absolute positioning accuracy of better than $100$ $\mu$m. Each calibration set consists of seven $z$ positions each with $22 \times 21$ corners at a $0.75$ mm spacing.

Reference measurements of droplet velocity and size were performed with a Dantec 2D-PDA System and a P80 processor. The PDA setup and evaluation parameters are similar to those published in [5].

| No. | $p_a\,[bar]$ | $T_a\,[K]$ | $U_{auv}\,[m/s]$ | $T_k\,[K]$ | $\dot{m}_k\,[g/s]$ | $q_{uv}$ | $\mathrm{We_{aero}}$ |
|---|---|---|---|---|---|---|---|
| 1 | 4 | 440 | 86 | 348 | 0.8 | 8 | 360 |
| 2 | 4 | 570 | 92 | 422 | 0.7 | 8 | 438 |
| 3 | 7 | 440 | 86 | 347 | 1.0 | 8 | 625 |
| 4 | 7 | 570 | 98 | 396 | 1.0 | 8 | 770 |

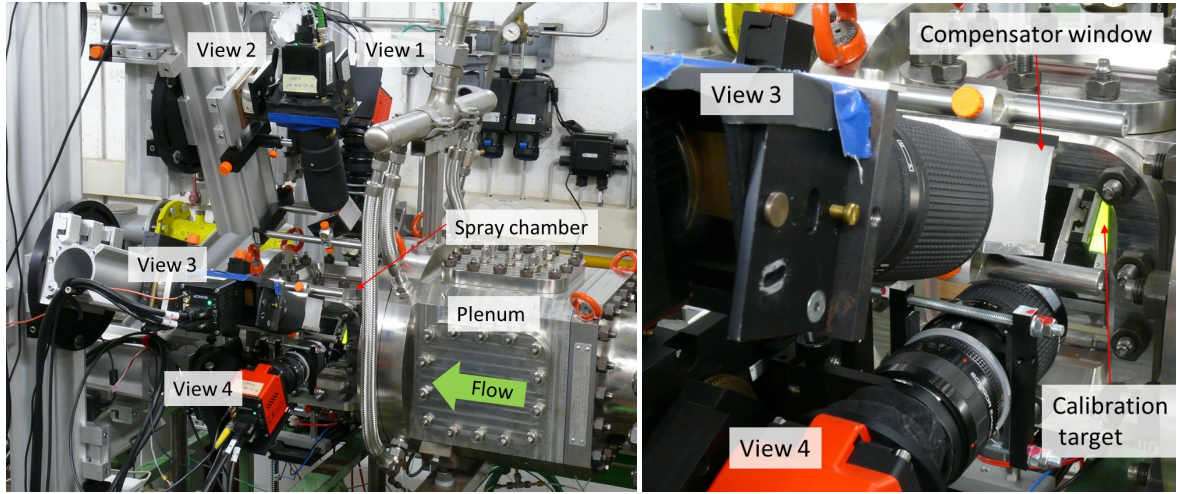**Table 1.** Operation conditions of single jet in cross-flow atomization

3

**Figure 4.** Optical swirling spray injector test rig and imaging setup; *Left* Camera arrangement; *Right* detail with calibration equipment

**Droplet image contrast and depth of field**

Tomographic shadowgraphy relies on shadow images or shadowgraphs of a spray field using polychromatic inline illumination with pulsed LED light. The term 'shadow image' does not fully address the involved processes because the absorption coefficient of kerosine for visible light is rather low ($5.0E - 07$ at $20°C$ and $1.7E - 6$ at $280°C$ [6]). Most of the photons impacting on the droplet are deflected by reflection, refraction and diffraction and images of small droplets appear as dark spots on a bright background because a major part of the deflected light is not captured by the imaging lens (see Fig. 5).

This raises the question on how the optical resolution and the further image processing influence the shadow image contrast and how the depth of field affects droplet visibility. PDA measurements $10$ mm downstream of the burner plate revealed kerosine droplet diameter ranging from $5 - 80$ $\mu$m for the base line case. However it is not obvious which part of this size fraction can be captured by tomographic shadowgraphy.

In the following the visibility of droplet shadows as a function of droplet size and volume position $z$ are estimated for the previously described multiple view setup. The underlying spray imaging model is based on a paper by Blaisot and Yon [7] who established the model to enable measurements of droplet sizes within diesel sprays using shadow images obtained from a single camera.

In the imaging model of Blaisot and Yon, the radial intensity distribution of a droplet shadow is modeled by the convolution of a slightly transmitting disc and the point spread function (PSF), with the latter describing the resolving capability of the imaging system. The point spread function is considered as a Gaussian and can be calibrated as a function of $z_{TS}$:

$$s(r, z_{TS}) = s_0 \, exp\left(-\frac{2r^2}{\chi^2(z_{TS})}\right),$$  (1)

where $s_0$ represents a normalization factor, $r$ is the radial droplet image coordinate and $\chi$ is the half-width.
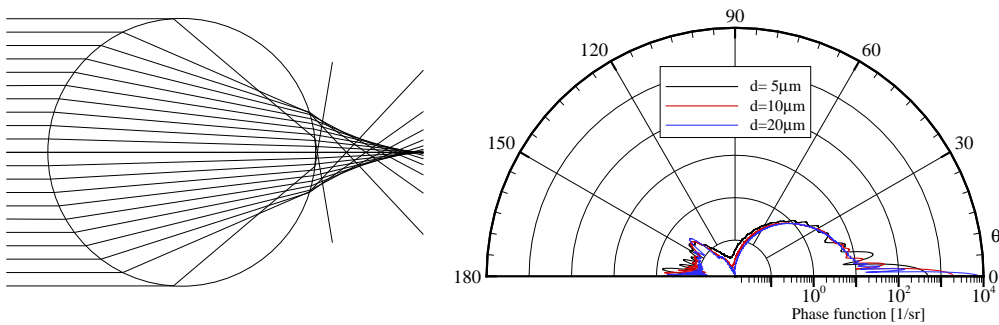


**Figure 5.** Light refraction inside a sphere (*left*) and Mie scattering of non-polarized polychromatic LED light ($\lambda = 460 - 600$ nm) upon spherical kerosine droplets in air (*right*)

4

The convolution of the slightly transmitting disc and the Gaussian PSF leads to:

$$i_n(\tilde{r}) = 1 - 2(1-\tau)\,exp(-\tilde{r}^2)\int_0^{\tilde{a}} exp(-\rho^2)\,I_0\,(2\tilde{r}\rho)\,d\rho\,, \qquad (2)$$

where $\tilde{r}$ is the non-dimensional radial image coordinate $\tilde{r} = \sqrt{2}r/\chi$ and $\tilde{a}$ is the non-dimensional droplet image radius $\tilde{a} = \sqrt{2}a/\chi$ both with regard to the half with of the PSF; $I_0$ is the Bessel function of the first kind and zero order and $\tau$ is the contrast coefficient. The latter refers to the disc transmission or Mie scattering within the bounds of the lens aperture. The estimation of the smallest visible droplets requires assumptions concerning the contrast coefficient $\tau$ which is gained from Mie simulations using MiePlot 4.5 [8].
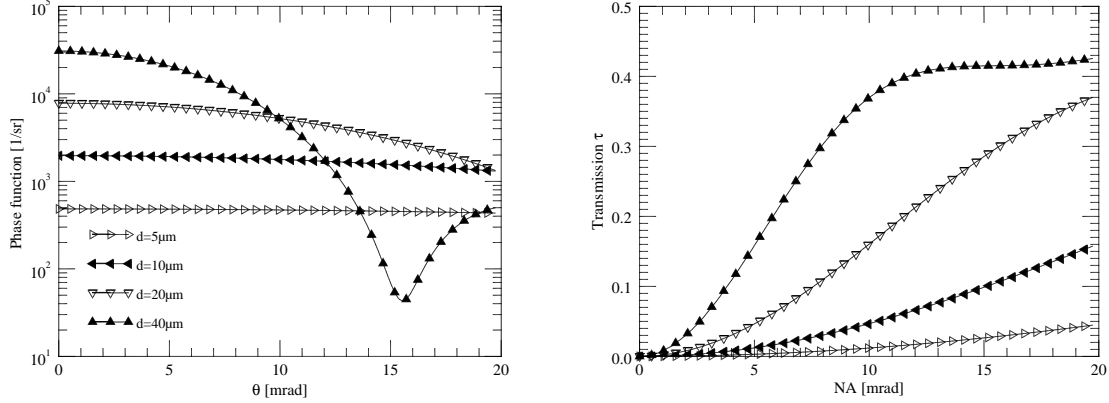


**Figure 6.** Forward-scattered intensity (*left*) versus scattering angle of non-polarized and polychromatic light ($\lambda = 460 - 600$ nm) upon spherical kerosine droplets in air ($T_k = 450K$, $T_a = 473K$) and droplet transmission (*right*) versus lens aperture

Fig. 6, left shows the simulated forward-scattered intensity as a function of scattering angle for polychromatic LED light ($\lambda = 0.46 - 0.60$ $\mu$m) of random polarization upon spherical kerosine droplets at temperatures of $T_k = 450K$ and air temperatures of $T_a = 473K$. The scattered intensity is expressed in terms of the so-called phase function which integrated over all scattering directions yields unity. While scattering by small droplets of $d = 10$ $\mu$m does not show a strong angle-dependency, larger droplets of $d = 50$ $\mu$m exhibit pronounced forward-scattering with a five times higher on-axis intensity and an additional intensity minimum at a scattering angle of $15.5$ mrad. If absorption is neglected, integration of the phase function over the solid angle of the camera aperture yields the droplet transmission versus lens aperture angle which is plotted in Fig. 6 (right). All four lenses were stopped down to $f_\# = 22$ which gives an aperture angle of $11$ mrad at a magnification of $M = 1$. At this numerical aperture, droplets of a diameter of $d = 10$ $\mu$m or $d = 50$ $\mu$m would have contrast coefficients of $0.05$ respectively $0.40$, so droplet transmission within the lens aperture has a strong droplet size dependency. Once the transmission coefficient is known, the image intensity profile of kerosine droplets of different sizes can be calculated. For example, Fig. 7 (left) shows image profiles at a width of the point spread function of $\chi = 10$ $\mu$m and a magnification of $M = 1$. Fig. 7 (right) shows the change of the intensity minimum of the image profile with droplet size for different PSF widths.

The remaining unknown is the width of the point spread function which was calibrated on the basis of intensity profiles across sharp edges (c.f. [9]). Therefore, chessboard calibration images were recorded at 13 $z_{TS}$ positions with $0.75$ mm spacing within the spray chamber. The images are flat-field corrected and back-projected into the volume to enable an estimation of the width of the overall point spread function in voxel-space which includes possible smoothing effects during reconstruction due to the finite voxel size and image interpolation. Fig. 8 (left) shows the intensity profile across chessboard edges (edge spread function) obtained from back projected calibration images of camera no. 1. The line spread function is obtained by numerical differentiation of the edge spread function [10]. The half-width of the line spread function is equal to the width of the PSF in $x$-direction and is obtained by matching the derived intensity profile with a Gaussian fit [11].

Fig. 9 (left) shows the half-width of the point spread functions for all views at a voxel sizes of $12$ $\mu$m (approx. $1.5$ voxel/pixel). The image sharpness of the inner views no. 2 and 3 decreases stronger towards the volume edges due to the longer focal length lenses ($f = 200$ mm instead of $f = 100$ mm) which leads to a decreased depth of focus. Only minor improvements can be achieved by decreasing the voxel size to $8$ $\mu$m (approx. $1.0$ voxel/pixel) because the resolution is limited by the optical arrangement.

On the basis of PSF calibrations and Mie simulations of the contrast coefficient the minimum intensity of the droplet image profiles can be calculated by the following equation (c.f. [7]):

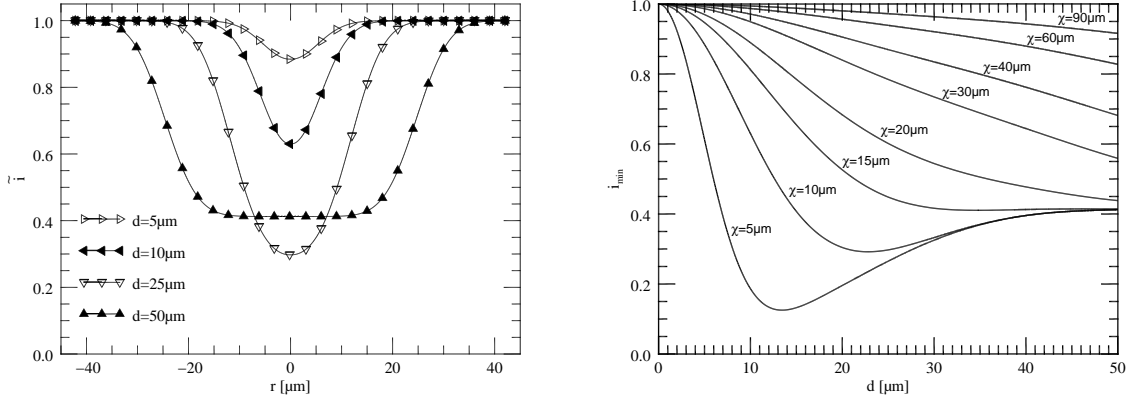$$\tilde{i}(0) = i_{min} = 1 - (1-\tau)(1 - exp(-\tilde{a}^2)). \qquad (3)$$

**Figure 7.** *Left:* Simulated shadow image profiles of kerosine droplets of different sizes at a PSF half-width of $\chi = 10\ \mu$m, $M = 1$, $f_\# = 22$. *Right:* Minimum intensity of droplet image profiles versus droplet size at different PSF half-widths at $M = 1$, $f_\# = 22$.

The minimum intensities of the droplets within the size range of $d = 5...80\ \mu$m are then compared to the smallest detectable intensity depletion of the spray background illumination in order to decide whether a droplet would be visible or not. This threshold of visibility is estimated from intensity fluctuations in 200 images recorded with LED light without spray. After image normalization, all pixel intensities have a mean of $\tilde{i} = 1 \pm \sigma$ and the threshold of visibility was set to a values of $\tilde{i} = 1 - 2\sigma$. The threshold estimations for view no. 1,2,3 and 4 yield the values $0.980$, $0.988$, $0.988$ and $0.980$. Fig. 9 (right) shows the estimated smallest visible droplet sizes in each view for a voxel size of $12\ \mu$m. If one of the views can not detect a droplet because of low contrast it would not be visible in the reconstructed volume. Therefore, the maximum of the size limits of all cameras gives the limit of the multiple view setup (red line in Fig. 9. The droplet visibility is only slightly improved if the voxel size is reduced to $8\ \mu$m (approx. 1 voxel/pixel) so a voxel size of $12\ \mu$m was chosen to reduce the computational time of volume processing as much as possible.

**Shadow image processing and volume reconstruction**
After dark image subtraction, shadowgraphs are median filtered within the $3 \times 3$ neighborhood to reduce pixel artifacts of the sCMOS camera sensor. The images are then flat-field corrected and normalized by division by a bright field image without spray. Prior to reconstruction the image intensities are inverted and a constant offset of $2\sigma$ is subtracted to clip intensities close to pixel noise (preprocessing **A**). The remaining unstructured background between droplet shadows (see Fig. 10, middle) seems to originate from small vaporized kerosine droplets with sizes below the smallest visible droplet size or from droplets which are out-of-focus. The remaining background around droplet images is partially removed by subtracting the local minimum in a $20 \times 20$ pixel kernel followed by clipping of a constant threshold (preprocessing **B**). The removal of unstructured background between droplet images is not complete because further increase of the threshold would clip droplet images of low contrast (see Fig. 10 bottom). Preprocessing **A** without sliding minimum subtraction and thresholding is applied prior reconstructions which are used to gain information about the placement of liquid phase in the spray ('volume fraction'). Preprocessing **B** is optimized to enhance gradients near the droplet shadow border and to improve the correlation signal for droplet velocity estimation.
The reconstructed volume size is $16 \times 13 \times 10$ mm³ which corresponds to $1312 \times 1088 \times 864$ voxel each having a size of $12\ \mu$m. The observed intensities from each voxel are reconstructed according to its line-of-sight intersection with each image plane. These positions are calculated from higher order mappings obtained from camera calibration as described in [12, 13]. Sub-pixel intensities are bilinearly interpolated between the 4-connected pixels. The observed intensities from each view are combined by a maximum entropy approach (MENT) [14, 15].
State-of-the-art cross-correlation processing is used for droplet displacement recovery in the volume [16, 17]. A multi-grid algorithm employ a resolution pyramid that starts at a rather coarse grid and stepwise increases resolution while continually updating a predictor field [18, 19]. To increase processing speed, factor $N$ volume down-sampling is applied by summing $N^3$ neighboring voxels. At a given resolution level integer-based sample offsetting is applied in a symmetric fashion using the estimate from the previous resolution step. Intermediate validation is based on normalized median filtering as proposed by Westerweel & Scarano [20]. Once the desired final spatial resolution is reached image or volume deformation based on third-order B-splines [21] is applied at least twice to further improve the match between volumes and thereby improving the displacement estimates. The final vector spacing is $0.38 \times 0.19 \times 0.19$ mm ($32 \times 16 \times 16$ voxel) at a interrogation volume size of $0.77 \times 0.38 \times 0.38$ mm ($64 \times 32 \times 32$ voxel). The processing for volume reconstruction and correlation is highly parallelized using OpenMP [22] to achieve optimal data throughput.
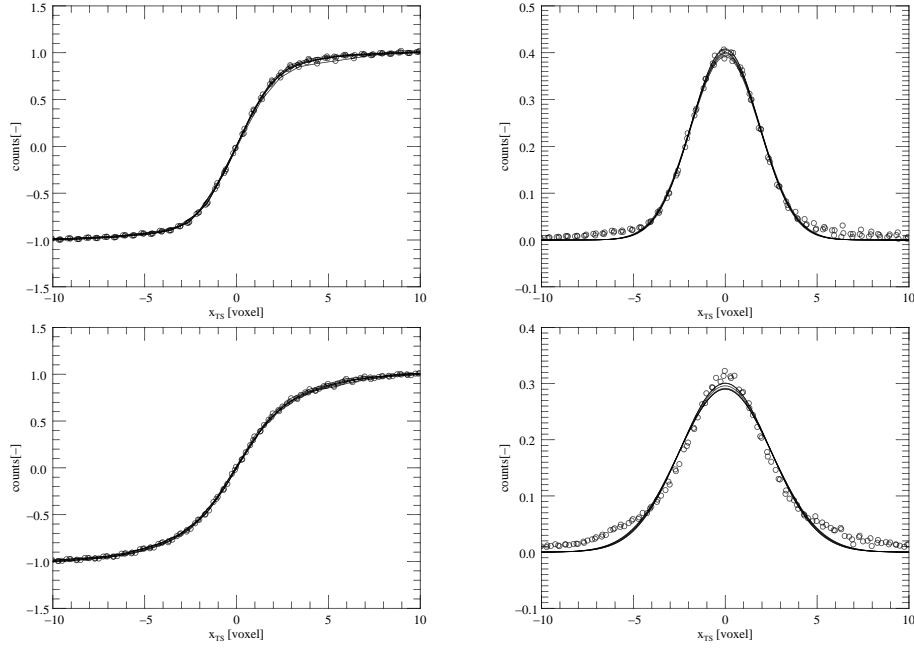
**Figure 8.** Quantification of edge response of the system along $x$ direction at a voxel size of $8$ $\mu$m obtained from chessboard images of view no. 1; edge spread (*left*) and line spread function plus Gaussian fit (*right*) in focus at $z = 0$ mm (*top*) and near the volume edge at $z = -4.5$ mm (*bottom*)
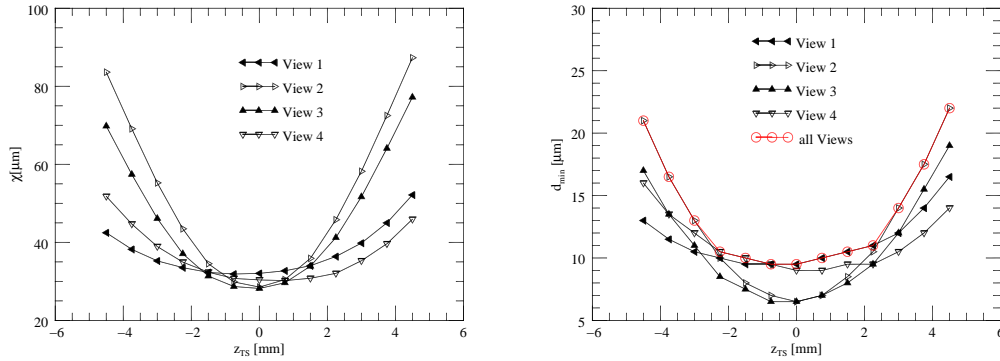


**Figure 9.** Calibration of the PSF of each camera (*left*) and smallest visible droplet diameter of the tomo shadow setup (*right*)

**Results and discussion**

The shadowgraph in Fig. 10 confirms that the spray is at a late state of air-blast atomization when it leaves the annular gap. There are some ligaments but most of the liquid is already dispersed into droplets. The droplet distribution is not homogeneous and wavy streaks of larger droplets appear in the jet. The dominant breakup mechanism of the kerosine jet should be *surface breakup* because the Weber number is close to the critical Weber number ($\mathrm{We}_{\mathrm{crit}} \simeq 10^{(3.1-log(q))/0.81}$=388 [23, 24]). During *surface breakup* ligaments and drops are continuously sheared-off of the jet surface mainly from the lateral sides of the jet. Below the critical Weber number *column breakup* is dominant where the liquid jet body breaks into larger irregular-shaped fragments and ligaments (c.f. [23, 25]).

Fig. 11 shows the intensity distribution within a spray volume at $p_A = 4$ bar, $T_A = 440$ K, $q_{uv} = 8$, $\mathrm{We}_{\mathrm{aero}} = 360$ at equidistant slices obtained from images after preprocessing **A**. Intensities are averaged over 150 samples to reduce the granularity from single droplet reconstructions. The average intensity distribution shows a u-shaped structure at ($x = 1 - 5$ mm) which indicates regions where droplets appear frequently. These regions seem to arise from the jet shear layer, where ligaments and drops are shed during surface breakup. Further downstream the windward leg of the u-shaped structure disintegrates faster possibly due to stronger interaction with the swirled flow. Reconstruction ambiguities ('ghost particles' [2]) lead to a slight elongation of the u-shaped structure along volume depth near the burner plate due to high droplet image densities. These ambiguities were also observed during earlier tomographic spray experiments with a similar camera setup [1]. Ambiguities could be partially suppressed by using additional cameras or advanced reconstruction algorithms which are subject of ongoing research.
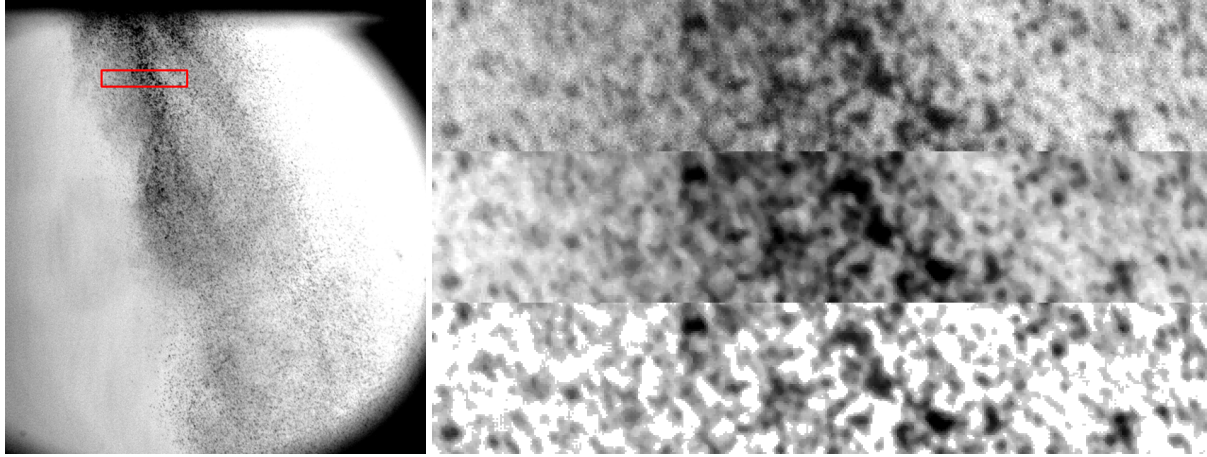
**Figure 10.** *Left*: Sample spray image obtained from view no. 1 at $p_A = 4$ bar, $T_A = 440$ K, $q_{uv} = 8$, $\mathrm{We_{aero}} = 360$. *Right*: Magnified region of $410 \times 80$ pixel ($\approx 3.11 \times 0.61$ mm ) obtained from the red box. Top: raw image; *Middle*: after contrast enhancement (processing **A**); *Bottom*: after local minimum subtraction ($20 \times 20$ neighborhood) and thresholding (processing **B**).
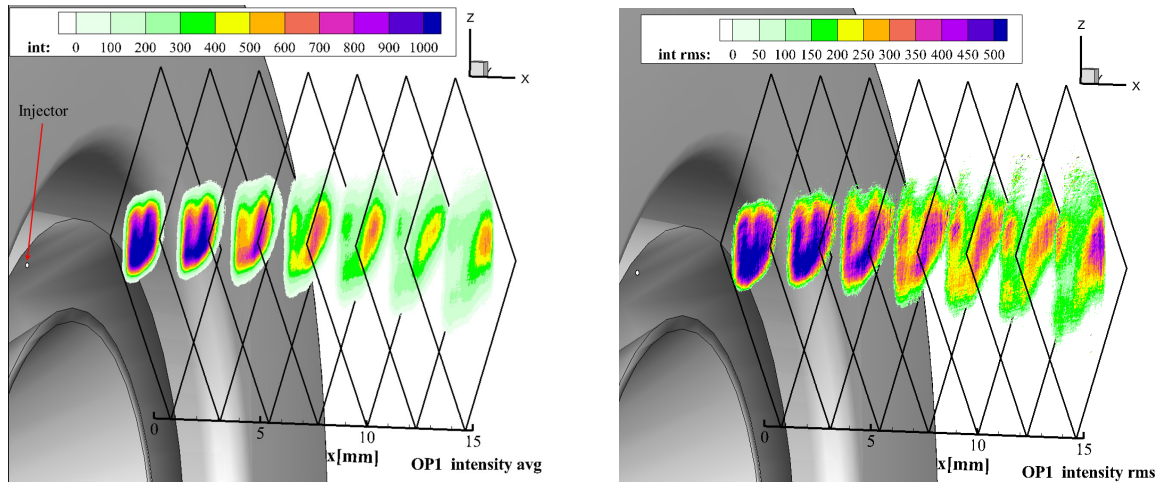


**Figure 11.** Average (*left*) and RMS (*right*) of 150 tomographic reconstructions at $p_A = 4$ bar, $T_A = 440$ K, $q_{uv} = 8$, $\mathrm{We_{aero}} = 360$

Interaction of the hot, pressurized air flow with the spray can be studied by single shot velocity fields obtained from 3D correlation of double volumes. Fig. 12 (top) shows equidistant slices of the velocity field obtained from single shot results at increasing Weber number. Correlation values below $10\%$ are blanked. The contour shape (axial velocity) can also be seen as a region, where droplets above the resolution limit of $d = 10$ $\mu$m appear in coherent motion. The contour size and position can be used to track the spray trajectory and extension in space at fixed time. The size of the contoured area clearly decreases with rising air and fuel temperature which indicates a significant droplet size reduction which is also evident from PDA measurements of liquid jet in cross flow atomization at elevated temperature (c.f. [26]).

Averaged spray velocities are shown in Fig. 13 and reveal slightly higher axial spray velocities on the windward side of the spray. There is a clear difference of the sizes of contoured areas (correlation coefficient above 10%) between instantaneous and time-averaged results at which indicates wide fluctuations of the spray tail position and extension. These differences are more pronounced at $T = 570$ K.

Near the burner plate both, instantaneous and time-averaged measurements show lower axial velocities inside the spray tail in comparison to outer regions. This might be due to the higher aerodynamic drag which the incoming air has to overcome until it reaches inner spray fragments, ligaments and droplets (c.f. [27]).

At $x = 10$ mm distance to the burner plate average velocities obtained from tomographic shadowgraphy are compared to 2D PDA measurements acquired along the dashed line in Fig. 2. Fig. 14 shows axial and tangential velocity profiles of different size classes in comparison with profiles obtained from 3d correlation of two reconstructed volumes. Axial velocities are in agreement with velocities obtained from the $d = 10$ $\mu$m and $d = 15$ $\mu$m size classes except in regions with strong gradients (e.g. $y = 7$ mm). Velocities obtained from 3D correlation drop off near the
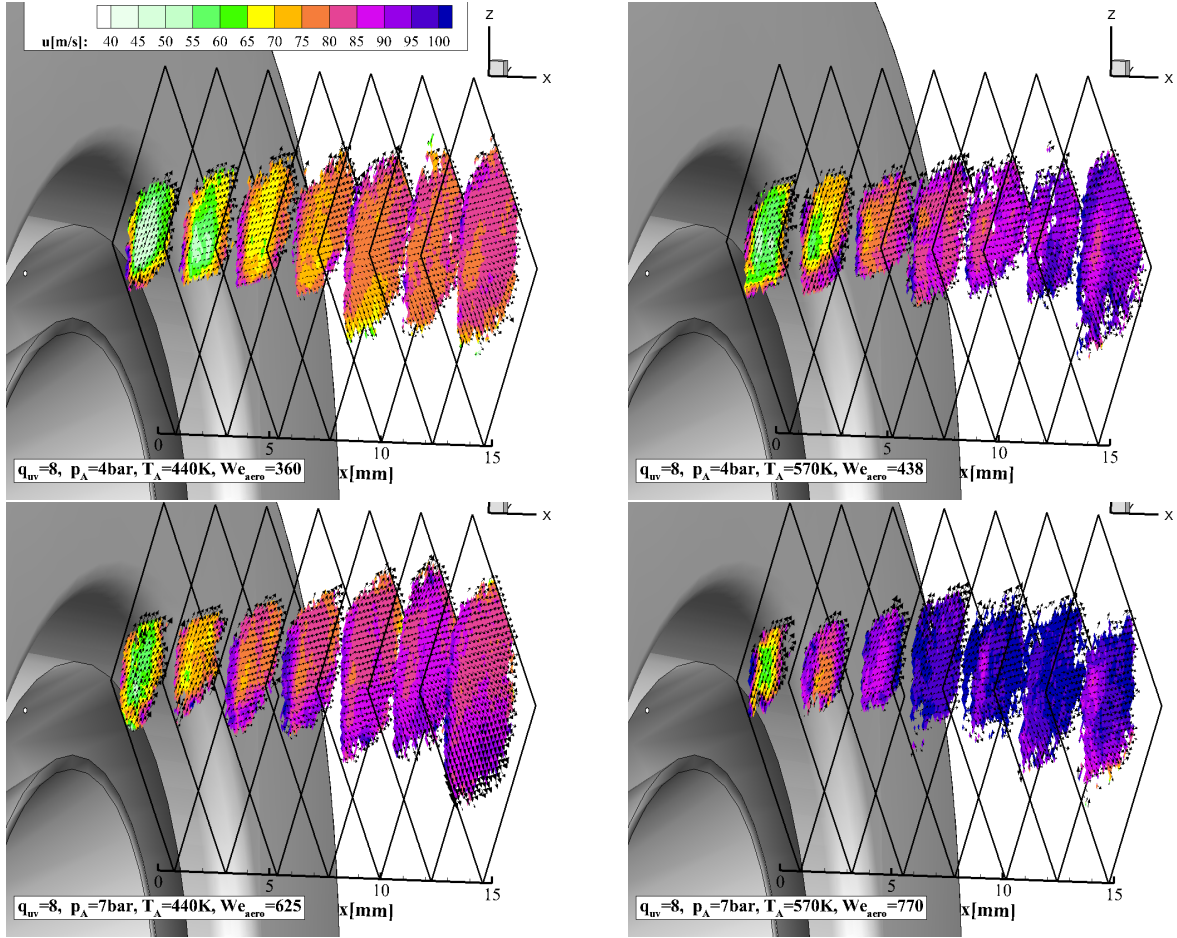
8

**Figure 12.** Snap shots of droplet velocities obtained from correlation of single shots. Vectors show the in-plane $v, w$ components.

edges, probably due to spatial averaging within the interrogation volume. Differences in tangential velocity are also present in regions with larger velocity gradients. There are two possible explanations for that: Either velocities are smoothed due to the correlation of varying droplet sizes within one interrogation volume or there is an additional bias due to reconstruction ambiguities ('ghost particles').

**Conclusions and outlook**

Tomographic shadowgraphy was successfully applied in a non-reactive kerosine spray in a pressurized environment with preheated swirled airflow. Measurements rely on the tomographic reconstruction of four views simultaneously imaging a volume of $16 \times 13 \times 10$ mm³ at a magnification close to unity using pulsed inline illumination. Estimations of the droplet shadow image contrast on the basis of PSF calibrations revealed that the depth of field strongly depends on droplet diameter. The minimum resolvable droplet diameter of the multiple view setup goes down to $d = 10$ $\mu$m within $-2$ mm $< z_{TS} < 2$ mm and than increases to $d = 10 - 20$ $\mu$m within the range 2 mm $< |z_{TS}| < 5$ mm.

Velocities of droplets above the resolution limit were retrieved by 3D correlation of small interrogation volumes of $0.77 \times 0.38 \times 0.38$ mm at vector spacing of $0.38 \times 0.19 \times 0.19$ mm. Three-dimensional instantaneous and time averaged spray velocities of jet-in-cross-flow atomization are measured at Weber numbers of $\mathrm{We_{aero}} = 360 - 770$, air pressures of $p_A = 4 - 7bar$ and air temperatures of $T_A = 440 - 570$ K. Extracted slices of the instantaneous axial velocity indicate strong motion (undulations) and fluctuations of the spray tail with increasing temperature. This shows clearly the advantage of instantaneous volumetric versus time averaged planar measurements which allow to visualize the trajectory of the spray tail in space at a fixed time. This could also be used to improve the estimates of time averaged kerosine volume fraction or dissipation rates by taking into account the temporal fluctuations of the spray placement.

To gain time resolved droplet velocities remains a challenging task because it would require acquisition rates in the order of $1/\Delta t = 0.6$ MHz accompanying with a significant reduction of the image resolution from $5$ Mpixel down to $30k$ Kpixel according to the state-of-the-art of imaging technology.
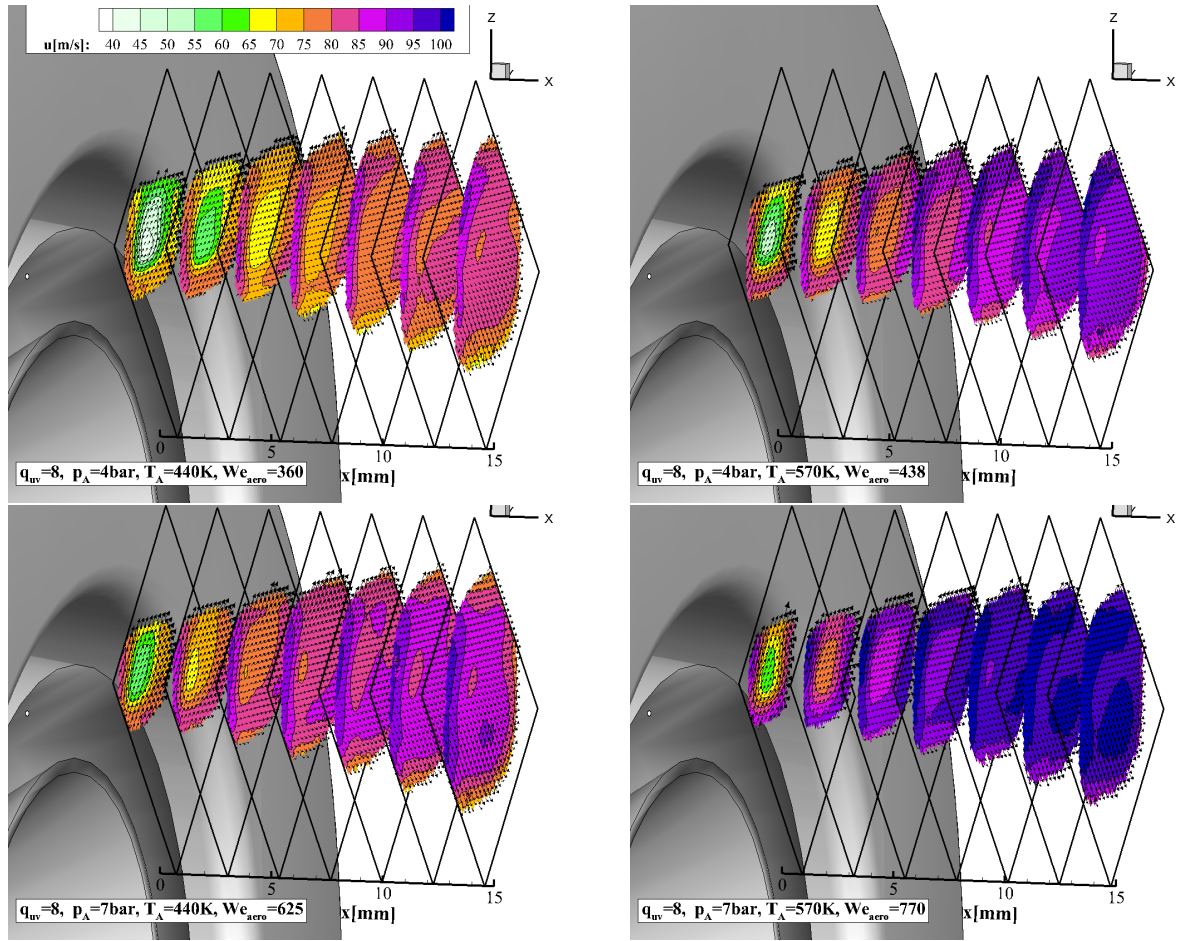
**Figure 13.** Droplet velocities obtained from (Vectors: in-plane $v, w$ components)
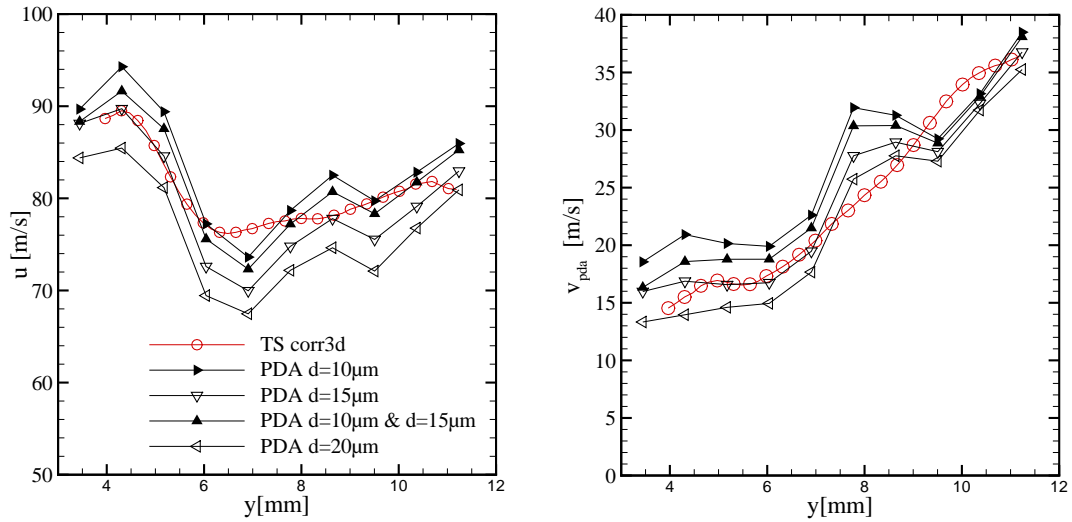


**Figure 14.** Comparison of PDA and TS velocity profiles obtained at $x = 10$ mm along the dashed line in Fig. 2 ($v_{pda}$ runs parallel to the dashed line), $p_A = 4$ bar, $T_A = 440$ K, $q_{uv} = 8$, $\text{We}_{\text{aero}} = 360$

10

**Nomenclature**

| | |
|---|---|
| $a, \tilde{a}$ | droplet radius, normalized radius $(= \sqrt{2}a/\chi)$ |
| d | droplet diameter |
| D | diameter of injection bore |
| f | focal length |
| $f_\#$ | f-number |
| $\tilde{i}$ | normalized image intensity |
| $I_{\mathrm{f,max}}$ | maximum continuous forward current |
| M | magnification |
| p | pressure |
| PDA | phase doppler anemometry |
| PSF | point spread function |
| $r, \tilde{r}$ | radial droplet image coordinate, normalized radial coordinate$(= \sqrt{2}r/\chi)$ |
| $\Delta t$ | delay between two illumination pulses |
| T | temperature |
| TS | tomographic shadowgraphy |
| q | liquid-to-air momentum flux ratio $(= \rho_k U_k^2/(\rho_a U_a^2))$ |
| U | velocity magnitude |
| u,v,w | velocity components along x,y,z |
| We | Weber number $= \rho U^2 D/\sigma$ |
| $\lambda$ | wavelength of light |
| $\nu$ | kinematic viscosity |
| $\rho$ | mass density or integration argument within the bounds $0 \leqslant \rho \leqslant \tilde{a}$ |
| $\sigma$ | standard deviation or surface tension |
| $\tau$ | droplet transmission in the bounds of lens aperture or contrast coefficient |
| $\tau_{\mathrm{p}}$ | pulse duration |
| $\chi$ | half-width of the point-spread function |
| $\varphi$ | camera yaw angle (around x axis) |

Subscripts

| | |
|---|---|
| a | air condition |
| k | kerosine condition |
| aero | computed with air flow properties |
| pda | basis for 2D-PDA vector space |
| ts | basis for TS vector space |
| uv | based on axial and tangential velocity components |

**References**

[1] J. Klinner and C. Willert. Tomographic shadowgraphy for three-dimensional reconstruction of instantaneous spray distributions. Experiments in Fluids, 53(2):531–543, 2012.

[2] G. Elsinga, F. Scarano, B. Wieneke, and B. van Oudheusden. Tomographic particle image velocimetry. Experiments in Fluids, 41:933–947, 2006.

[3] S. Freitag and T. Behrendt. Commissioning of the optical swirling spray injector: A new test section for investigations of atomization inside an aero engine burner at realistic operating conditions. In I26th European Conference Liquid Atomization & Spray Systems (ILASS), 08.-10. Sept. 2014, Bremen, Germany, 2014.

[4] Christian Willert, Boleslaw Stasicki, Joachim Klinner, and S. Moessner. Pulsed operation of high-power light emitting diodes for imaging flow velocimetry. Measurement Science and Technology, Vol. 21(7):1–12, 2010.

[5] Stefan Freitag, U. Meier, Johannes Heinze, Thomas Behrendt, and Christoph Hassa. Measurement of initial conditions of a kerosene spray from a generic aeroengine injector at elevated pressure. Atomization and Sprays, 21(6):521–535, 2011.

[6] M. Rachner. Die Stoffeigenschaften von Kerosin Jet A-1. Technical Report ISRN DLR-FB-98-01, DLR, 1998.

[7] J. B. Blaisot and J. Yon. Droplet size and morphology characterization for dense sprays by image processing: application to the diesel spray. Experiments in Fluids, 39(6):977–994, 2005.

[8] Philip Laven. Simulation of rainbows, coronas, and glories by use of mie theory. Appl. Opt., 42(3):436–444, Jan 2003.

[9] R. Clark Jones. On the point and line spread functions of photographic images. J. Opt. Soc. Am., 48(12):934–937, Dec 1958.

$f_\#$

[10] Christopher D. Claxton and Richard C. Staunton. Measurement of the point-spread function of a noisy imaging system. J. Opt. Soc. Am. A, 25(1):159–170, Jan 2008.

[11] U. V. Gopala Rao and V. K. Jain. Gaussian and exponential approximations of the modulation transfer function. J. Opt. Soc. Am., 57(9):1159–1160, Sep 1967.

[12] S M Soloff, R J Adrian, and Z-C Liu. Distortion compensation for generalized stereoscopic particle image velocimetry. Measurement Science and Technology, 8(12):1441, 1997.

[13] J. Klinner and C. Willert. Application of tomographic piv in a transonic cascade. In 10th International Symposium on Particle Image Velocimetry – PIV 13, July 2013.

[14] Gerald Minerbo. Ment: A maximum entropy algorithm for reconstructing a source from projection data. Computer Graphics and Image Processing, 10(1):48 – 68, 1979.

[15] A V Bilsky, V A Lozhkin, D M Markovich, and M P Tokarev. A maximum entropy reconstruction technique for tomographic particle image velocimetry. Measurement Science and Technology, 24(4):045301, 2013.

[16] M. Raffel, C. Willert, S. Wereley, and J. Kompenhans. Particle Image Velocimetry, A Practical Guide. Springer Berlin-Heidelberg, 2007.

[17] J. Westerweel, D. Dabiri, and M. Gharib. The effect of a discrete window offset on the accuracy of cross-correlation analysis of digital piv recordings. Experiments in Fluids, 23(1):20–28, 1997.

[18] F Scarano. Iterative image deformation methods in piv. Measurement Science and Technology, 13(1):R1, 2002.

[19] S. T. Wereley and C. D. Meinhart. Second-order accurate particle image velocimetry. Experiments in Fluids, 31(3):258–268, 2001.

[20] Jerry Westerweel and Fulvio Scarano. Universal outlier detection for PIV data. Experiments in Fluids, 39(6):1096–1100, 2005.

[21] P. Thévenaz, T. Blu, and M. Unser. Interpolation revisited. IEEE Transactions on Medical Imaging, 19(7):739–758, July 2000.

[22] OpenMP Architecture Review Board. OpenMP application program interface version 4.5, November 2015.

[23] Pei-Kuan Wu, Kevin A. Kirkendall, Raymond P. Fuller, and Abdollah S. Nejad. Breakup processes of liquid jets in subsonic crossflows. Journal of Propulsion and Power, 13(1):64–73, January 1997.

[24] Julian Becker and Christoph Hassa. Breakup and atomization of a kerosene jet in crossflow at elevated pressure. Atomization and Sprays, 12(1-3):49–67, 2002.

[25] Mohsen Behzad Jazi. Surface Breakup of A Liquid Jet Injected Into A Gaseous Crossflow. PhD thesis, Graduate Department of Civil Engineering, University of Toronto, 2014.

[26] C. Hassa and P.F. Wiesmath. The effect of initial fuel temperature on vaporization in aero engine combustors with prevaporization. In ICLASS 2012, 12th Triennial International Conference on Liquid Atomization and Spray Systems, Heidelberg, Germany, September 2-6, 2012.

[27] Pei-Kuan Wu, Kevin A. Kirkendall, Raymond P. Fuller, and Abdollah S. Nejad. Spray structures of liquid jets atomized in subsonic crossflows. Journal of Propulsion and Power, 14(2):173–182, March 1998.